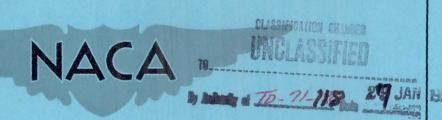
Copy 436 RM L58A16

in radeo at 5 year



RESEARCH MEMORANDUM

Declassified by authority of NASA Classification Change Notices No. 2 1 2 Dated ** 1-MAR 1971

INVESTIGATION OF TWO BLUFF SHAPES IN AXIAL FREE FLIGHT

OVER A MACH NUMBER RANGE FROM 0.35 TO 2.15

By Lucille C. Coltrane

Langley Aeronautical Laboratory
Langley Field, Va.







NATIONAL ADVISORY COMMITTEE FOR AERONAUTICS

WASHINGTON

March 18, 1958

NACA RM L58A16

1



NATIONAL ADVISORY COMMITTEE FOR AERONAUTICS

RESEARCH MEMORANDUM

INVESTIGATION OF TWO BLUFF SHAPES IN AXIAL FREE FLIGHT

OVER A MACH NUMBER RANGE FROM 0.35 TO 2.15

By Lucille C. Coltrane

SUMMARY

A fineness-ratio-2.71 right circular cylinder and a fineness-ratio-4.0 circular cylinder with a rounded nose and a flared afterbody have been tested in free flight over a Mach number range of 0.35 to 2.15 and a Reynolds number range of 1×10^6 to 12×10^6 . Time histories, cross plots of force coefficients, rolling velocity, and longitudinal-force coefficient are presented for both cylinders. In addition, cross plots of moment coefficients and plots of the normal-force curve slope and the aerodynamic center are presented for the fineness-ratio-2.71 cylinder. The average aerodynamic center of the right circular cylinder moved rearward with decreasing speeds until at the subsonic Mach numbers it remained approximately constant and comparisons of the drag data of this test with wind tunnel and other free-flight data show good agreement. An appreciable decrease in drag was observed when the data of the present test of the rounded nose cylinder were compared with data of a right circular cylinder of a similar configuration.

INTRODUCTION

The dynamic stability characteristics of shapes having very high drag and very low lift are of interest to designers of various aerodynamic stores (see refs. 1 and 2) and shapes such as a reentry missile. One configuration which meets these requirements is the circular cylinder in axial flow. An investigation is being conducted by the Langley Pilotless Aircraft Research Division with the rocket-boosted free-flight-model technique to obtain stability data on bluff shapes in axial free flight.

The present investigation was conducted to extend the data in reference 3 to higher Mach numbers and to determine the effect of a change in nose shape on the aerodynamic characteristics of a bluff shape. For this purpose flight tests were made of two additional cylinders, a right





circular cylinder with a fineness ratio of 2.71 of the same design as the fineness-ratio-2.56 cylinder of reference 3 and a circular cylinder with a rounded nose and a flared afterbody of the same design except for nose shape as the fineness-ratio-4.0 cylinder of reference 3. The results of these flight tests are presented in this paper. These tests covered a Mach number range from 0.35 to 2.15 and a Reynolds number range from 1 \times 10 6 to 12 \times 10 6 based on cylinder diameter. The free-flight tests were conducted at the Langley Pilotless Aircraft Research Station at Wallops Island, Va.

SYMBOLS

The data are presented relative to the body axis system and the positive directions of the force coefficients, moment coefficients, and angular velocities are shown in figure 1. The various symbols used throughout the paper are defined as follows:

a accelerometer reading, g units

$$C_{C}$$
 longitudinal-force coefficient, $a_{l,cg} \frac{W/S}{q}$

$$C_{m}$$
 pitching-moment coefficient, $\frac{I_{Y}}{qSd}(\ddot{\theta} - \dot{\psi}\dot{\phi})$

$$C_{m_{q}} = \frac{dC_{m}}{d\frac{\dot{\theta}d}{2V}}$$

$$C_{N}$$
 normal-force coefficient, $a_{n,cg} \frac{W/S}{q}$

$$C_{N_{\alpha}} = \frac{dC_{N}}{d\alpha}$$

$$C_n$$
 yawing-moment coefficient, $\frac{I_Z}{qSd}(\ddot{\psi} + \dot{\theta}\dot{\phi})$

$$c_{Y}$$
 lateral-force coefficient, $a_{t,cg} \frac{W/S}{q}$



g	acceleration due to gravity, ft/sec2
I	moment of inertia, slug-ft ²
I_X , I_Y , I	moments of inertia, slug-ft ²
k	radius of gyration, $\sqrt{\frac{I_{\underline{Y}}}{m}}$, ft
ı	length of cylinder, ft
М	Mach number
m	mass, slug
q	dynamic pressure, lb/sq ft
R	Reynolds number based on cylinder diameter
r	radius of cylinder nose, in.
S	cross-sectional area of cylinder, sq ft
t	time, sec
V	free-stream velocity, ft/sec
W	weight of cylinder, lb
х	distance along cylinder from nose, ft, or, when used with a subscript, distance from center of gravity, positive forward, ft
θ	angle of pitch
λ0	nonrolling damping constant, 1/sec
Δλ	damping constant due to roll, 1/sec
μ	relative-density factor, $\frac{4m}{\rho Sd}$
ρ	air density, slugs/cu ft
φ	angle of roll, radians

angle of yaw, radians



 ω_{Ω} basic oscillation frequency, radians/sec

component of total pitch frequency resulting directly from roll, radians/sec

 $\ddot{\theta}$ - $\dot{\psi}\dot{\phi}$ pitching acceleration, g $\frac{a_{n,2} - a_{n,1}}{x_{n,2} - x_{n,1}}$, radians/sec²

a_{n,cg} normal acceleration, $\frac{a_{n,1}x_{n,2} - a_{n,2}x_{n,1}}{x_{n,2} - x_{n,1}}$, g units

... $\psi + \theta \varphi$ yawing acceleration, $g \frac{a_{t,2} - a_{t,1}}{x_{t,2} - x_{t,1}}$, radians/sec²

 $a_{t,cg}$ transverse acceleration, $\frac{a_{t,1}x_{t,2} - a_{t,2}x_{t,1}}{x_{t,2} - x_{t,1}}$, g units

Subscripts:

ac aerodynamic center

cg center of gravity

l longitudinal

n normal

t transverse

tot total

1 forward end of cylinder

2 rear end of cylinder

A dot above a symbol indicates time rate of change of symbol, for example, $\dot{\theta} = \partial \theta / \partial t$.

MODELS

The physical characteristics of the models are presented in table I, and drawings of the models are shown in figure 2. Photographs of the models and model booster arrangements are presented in figure 3.



The fineness-ratio-2.71 model (designated model I) was a right circular cylinder with a diameter of 8 inches and contained two small rockets which were mounted normal to the longitudinal axis and ahead of the center of gravity to give a yaw disturbance. The center of gravity of this model was located at 34.3 percent of the cylinder length behind the nose. The fineness-ratio-4.0 model (designated model II) was a circular cylinder with a diameter of 8.0 inches, a 13° flared afterbody, and a rounded nose and contained no small rockets. The afterbody and nose lengths are shown in figure 2 and the contour ordinates for the nose are shown in table II. The center of gravity of this model was located at 24.5 percent of the model length behind the nose.

The cylindrical portions of the models were constructed of steel and were covered with a fiber-glass plastic shell. The forward portion of model I and the nose of model II were machined from solid steel. The afterbody flare of model II was constructed of laminated wood.

INSTRUMENTATION

Model instrumentation consisted of an NACA six-channel telemeter which transmitted data from six accelerometers located as follows: one normal and one transverse accelerometer in the forward end of the cylindrical portion of the model, one normal and one transverse accelerometer in the rear of the cylindrical portion of the model, and two longitudinal accelerometers, one for high range and one for low range, behind the center of gravity. A measure of the signal strength transmitted from the loop antenna provided an indication of the roll rate of the cylinders since the strength of the signal varied with the cylinder roll position.

Ground instrumentation included a CW Doppler radar unit to measure the velocity of the model, a modified SCR 584 tracking radar set to determine the flight path and a rollsonde receiver used as an additional measure of the rolling velocity. Fixed and tracking motion-picture cameras were used to observe the model during the first portion of the flight. Atmospheric data were obtained from a rawinsonde released immediately before model flight.

TESTS AND ANALYSIS

Tests

The models were ground launched at an angle of 70° from the horizontal by means of a mobile launcher as shown in figure 3(c). A solid-fuel Cajun rocket motor boosted the models to maximum velocity. Drag



flaps were incorporated into the booster to increase the separating force between the model and booster at booster burnout. For model I, the drag flaps operated as designed, but, for model II, motion pictures showed the drag flaps opened prematurely, came off, and damaged the booster fins. The damaged fins probably increased the drag of the booster and, although separation was delayed about 0.3 second, a clean separation was experienced. In addition, the damaged booster fins caused the model-booster combination to experience a high rolling velocity immediately before separation. This high rolling velocity persisted throughout the flight of the model. Tracking radar showed that the models followed an approximately parabolic flight path.

Analysis

As was done in reference 4, the method of analysis used herein to determine the pitching-moment coefficients consists of using the data obtained from normal accelerometers located at two positions in the model. When the normal-force equation is combined with the equation describing the normal-accelerometer reading at any point along the x-axis of the model, it can be shown that

$$\frac{g}{x_{n,2} - x_{n,1}} (a_{n,2} - a_{n,1}) = \ddot{\theta} - \dot{\psi}\dot{\phi}$$
 (1)

The pitching-moment equation may be written as

$$qSdC_{m_{tot}} = I_{Y}\ddot{\theta} - (I_{Z} - I_{X})\dot{\phi}\dot{\psi}$$
 (2)

if I_{XZ} = 0. Now, if I_Y = I_Z as is the case for the models reported herein (see table I),

$$qSdC_{m_{tot}} = I_{Y}(\ddot{\theta} - \dot{\phi}\dot{\psi}) + I_{X}\dot{\phi}\dot{\psi}$$
 (3)

and then, if $I_X \dot{\phi} \dot{\psi}$ is small with respect to $I_Y (\ddot{\theta} - \dot{\phi} \dot{\psi}),$

$$C_{m_{tot}} = \frac{I_{Y}}{qSd} (\mathring{\theta} - \mathring{\phi} \mathring{\psi})$$
 (4)

For model I, equation (4) may be used directly since the roll rate was found to be small and the term $I_X \phi \dot{\psi}$ can be neglected.



For the aerodynamic-center location, where

$$x_{ac} = \frac{dC_m}{dC_N} \frac{d}{l} + \frac{x_{cg}}{l}$$

or

$$x_{ac} = \frac{dC_n}{dC_v} \frac{d}{l} + \frac{x_{cg}}{l}$$

the values for $\frac{dC_m}{dC_N}$ and $\frac{dC_n}{dC_Y}$ were taken directly from the polars of C_m against C_N and C_n against C_Y at C_N or C_Y near zero.

In order to determine the normal-force coefficient curve slope as presented herein for model I and for the fineness-ratio-2.56 cylinder of reference 3, equation (42) in reference 5, which states that

$$C_{N_{\alpha}} = \frac{-2\mu \left(\frac{x_{2}}{d} - \frac{x_{1}}{d}\right) \left(\frac{d}{2V}\right)^{2}}{s} \left[\omega_{0}^{2} + \lambda_{0}^{2} - \Delta\lambda^{2} + \Delta\omega^{2} \frac{I_{X}}{I} \left(1 - \frac{I_{X}}{I_{I}}\right)^{2}}{\left(1 - \frac{I_{X}}{2I}\right)^{2}}\right]$$
(5)

was simplified by omitting the damping terms. Analysis of the data that were obtained after the firing of the two pulse rockets showed that the last three terms within the brackets were small when compared with the term of the basic oscillation frequency $\omega \mathcal{G}$. (See table III.) Therefore, they were neglected throughout the calculation. Then by the relation

$$s = \frac{\left(\frac{x_2}{d} - \frac{x_1}{d}\right)}{(k/d)^2} \frac{dC_m}{dC_N}$$
 (6)

it is possible to express $\text{C}_{N_{\text{CL}}}$ in terms of $\frac{\text{d}\text{C}_{m}}{\text{d}\text{C}_{N}}$ as follows:

$$C_{N_{\alpha}} = \frac{-2\mu \left(\frac{d}{2V}\right)^{2} \left(\frac{k}{d}\right)^{2}}{\frac{dC_{m}}{dC_{N}}} \left(\omega_{0}^{2}\right)$$
 (7)

The slopes $\frac{dC_m}{dC_N}$ and $\frac{dC_n}{dC_Y}$ were equal for the polars of model I. Since variations of C_N and α were probably nonlinear, this average C_{N_α} may be greater or less than values near $C_N=0$, depending upon the range of C_N encountered in flight.

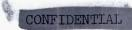
An indication of the dynamic stability following the disturbance given the model by the pulse rockets was obtained through the use of equation (43) in reference 5, where

$$c_{m_q} = 2\left(\frac{k}{d}\right)^2 \left(\frac{2\mu d}{2V} \lambda_0 + c_{N_\alpha}\right) \tag{8}$$

ACCURACY

The instrument inaccuracies, estimated to be ±2 percent of their calibrated range, are stated in coefficient form for representative Mach numbers as follows:

Coefficient	Fineness-ratio-2.71 model (model I) at Mach numbers of -			Fineness-ratio-4.00 model (model II) at Mach numbers of -		
	1.88	1.26	0.80	2.00	1.38	0.80
$^{\mathrm{C}}\mathrm{_{N}}$	±0.039	±0.094	±0.250	±0.038	±0.085	±0.309
$C_{\underline{Y}}$	±0.040	±0.095	±0.254	±0.039	±0.087	±0.316
$C_{\mathbb{C}}$	±0.051	±0.030	±0.079	±0.052	±0.030	±0.104



2



PRESENTATION OF RESULTS

The variation of test Reynolds number, based on cylinder diameter, with test Mach number is presented in figure 4. The model flight paths are presented as plots of altitude against horizontal distance in figure 5 and the variation of velocity and dynamic pressure with time is shown in figure 6.

Time histories of the normal-force coefficient, lateral-force coefficient, and Mach number are presented in figures 7 and 8. Basic data cross plots of force and moment coefficients for model I are shown in figure 9. Examples of the variation of the normal-force coefficient with lateral-force coefficient for model II are shown in figure 10. An indication of the rolling velocity against Mach number is shown in figure 11. For model I, as a function of Mach number, the variation of the average aerodynamic center in cylinder lengths behind the nose is presented in figure 12, and the normal-force curve slope is presented in figure 13. The measured longitudinal-force coefficient for both models is plotted against Mach number and is presented in figure 14.

DISCUSSION OF RESULTS

Time History

A time history of M, $C_{\rm N}$, and $C_{\rm Y}$ for model I is shown in figure 7. A disturbance at separation (t = 2.85) caused the instruments to exceed their calibrated ranges at each oscillation peak for about 1 second. Throughout the flight a coupled motion with respect to the body axis system was experienced by the model as the oscillations damped from large amplitudes at supersonic speeds to low amplitudes at subsonic speeds. Figure 8 presents a time history of M, $C_{\rm N}$, and $C_{\rm Y}$ for model II.

Basic Data Plots

Plots of $C_{\rm N}$ against $C_{\rm Y}$ presented in figures 9 and 10 for various Mach numbers indicate the model motion. When the trim center is estimated, the time history of the resultant force vector can be obtained and the angular displacement of adjacent peaks gives an indication of the rolling rate. This use of the $C_{\rm N}$ and $C_{\rm Y}$ cross plots is discussed in detail in reference 5. Also, as stated in reference 5, whether the missile is above or below roll resonance is immediately determined, since the motion above resonance is characterized by inside loops, and the motion below roll



resonance by outside loops. Therefore, it can be seen that model I was below roll resonance and model II was above roll resonance; in fact, by comparing the plot of $C_{\rm N}$ against $C_{\rm Y}$ of figure 10 with a similar plot in figure 5 of reference 5, it is apparent that model II rolled at a rate of about three times the pitch frequency. This ratio is nearly the same as the ratio of the measured roll rate of model II and the nonrolling pitch frequency of a nearly similar fineness ratio 4.0 cylinder of reference 3. Dashed lines in figure 9 indicate extrapolated values where the range of the instruments was exceeded but these data points were considered accurate enough for obtaining an estimate of the roll rate. This estimate is shown with measured averages from the rollsonde in figure 11 and good agreement is noted.

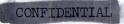
Figure 9 shows that the variation of moment coefficient with force coefficient for model I was nonlinear in both the pitch and yaw planes, the greatest stable slope generally occurring at the zero force coefficient. An attempt was made to determine the stability characteristics for model II from the disturbance received at separation; however, the scatter of data for the plots of C_m against C_N and C_n against C_Y prohibited the determination of a slope $\mathrm{d} C_m/\mathrm{d} C_N$ to be used in equation (6). Thus neither $C_{N_{\mathrm{CL}}}$ nor the aerodynamic-center location could be determined. The relative importance of the various terms within the brackets of equation (5) for a model rolling about 100 radians/sec can be noted in table III for model II.

Aerodynamic Center

The variation of the aerodynamic center with Mach number for model I is shown in figure 12. The average aerodynamic center moved rearward as the speed decreased through the supersonic and transonic speeds but remained at a constant position of about 0.64 cylinder lengths behind the nose through the subsonic range. For comparison, a dashed-line curve faired from data of the fineness-ratio-2.56 cylinder of reference 3 is also presented in figure 12. The comparison is considered good especially when the accuracies in the basic data are taken into account.

Lift

The variation of the normal-force curve slope with Mach number for model I is shown in figure 13. It is seen that ${\rm C}_{\rm N_{\rm C}}$ decreased with decreasing speeds until at subsonic Mach numbers it remained approximately constant. Also shown in figure 13 is a curve of ${\rm C}_{\rm N_{\rm C}}$ from faired data of the fineness-ratio-2.56 model of reference 3 which shows good agreement.





With $C_{N_{\rm C}}$ known, $C_{\rm m_q}$ was calculated to be -26 per radian at M = 1.03 and 22 per radian at M = 0.70. Since the term $\lambda_{\rm O}$ is small (see table III) and in these flight tests is difficult to obtain with good accuracy, these values should be considered as good estimates and not absolute values of the dynamic stability at these Mach numbers.

Drag

The variation of longitudinal-force coefficient with Mach number for the models of the present tests is presented in figure 14. The shaded areas on the figures indicate values of $C_{\rm C}$ obtained for all $C_{\rm N}$ and $C_{\rm Y}$ values of the tests. Also presented are the drag data for both models when $C_{\rm N}<0.1$ and $C_{\rm Y}<0.1$. For model I, comparison of these data with the drag of the fineness-ratio-2.56 cylinder of reference 3 when $C_{\rm N}<0.1$ and $C_{\rm Y}<0.1$ and the drag data of reference 6 for the body of revolution where r=0.00 inch shows good agreement. Comparison of the data of model II with the data of the fineness-ratio-4.0 cylinder with flared afterbody of reference 3 when $C_{\rm N}<0.1$ and $C_{\rm Y}<0.1$ indicates that a considerable reduction in drag throughout the Mach number range was obtained by the nose modification of the present test. The drag data of model II and the drag data of reference 6 (where r=0.50 inch) show reasonable agreement at subsonic speeds.

CONCLUDING REMARKS

A fineness-ratio-2.71 right circular cylinder and a fineness-ratio-4.0 cylinder with a rounded nose and a flared afterbody have been tested in rocket-boosted axial free flight over a Mach number range of 0.35 to 2.15 and a Reynolds number range of 1×10^6 to 12×10^6 . When given a disturbance at supersonic speeds, the response of the fineness-ratio-2.71 cylinder was a large-amplitude oscillation which damped to a low-amplitude sustained oscillation at subsonic speeds. The model experienced a low roll rate throughout the test. This value was less than the roll rate required for resonance. The moment-force curves were nonlinear, with greatest stable slope generally occurring at the zero force coefficient. The average aerodynamic center moved rearward and the normal-force curve slope decreased with decreasing speeds until at the subsonic Mach numbers they remained approximately constant. Comparisons of the drag data of this test with wind-tunnel and other free-flight data show good agreement. The fineness-ratio-4.0 cylinder experienced a high rate of roll throughout the test. This value was considerably more than the roll rate required



for resonance. An appreciable decrease in drag was observed when the data of the present test of a rounded nose cylinder were compared with data of a right circular cylinder of a similar configuration.

Langley Aeronautical Laboratory,
National Advisory Committee for Aeronautics,
Langley Field, Va., December 30, 1957.

REFERENCES

- 1. Walchner, Otto, Weigand, Heinrich, and Kroeger, Hermann: Dynamic Stabilizer for the Finless Bluff Bomb. Tech. Note WCRR 54-53, Wright Air Dev. Center, U. S. Air Force, Apr. 19, 1954.
- 2. Carter, Howard S., and Lee, John B.: Investigation of the Ejection Release of Several Dynamically Scaled Bluff Internal Stores at Mach Numbers of 0.8, 1.39, and 1.98. NACA RM L56H28, 1956.
- 3. McFall, John C., Jr.: Dynamic Stability Investigation of Two Right Circular Cylinders in Axial Free Flight at Mach Numbers From 0.4 to 1.7 Fineness-Ratio-2.56 Cylinder and Fineness-Ratio-4.0 Cylinder With Flared Afterbody. NACA RM L56L28, 1957.
- 4. Peck, Robert F., and Coltrane, Lucille C.: Longitudinal Characteristics at Transonic and Supersonic Speeds of a Rocket-Propelled Airplane Model Having a 60° Delta Wing and a Low Swept Horizontal Tail. NACA RM L55F27, 1955.
- 5. Nelson, Robert L.: The Motions of Rolling Symmetrical Missiles Referred to a Body-Axis System. NACA TN 3737, 1956.
- 6. Polhamus, Edward C.: Effect of Nose Shape on Subsonic Aerodynamic Characteristics of a Body of Revolution Having a Fineness-Ratio of 10.94. NACA RM L57F25, 1957.





TABLE I.- PHYSICAL CONSTANTS FOR CYLINDERS TESTED

Constant	Model I	Model II
W, 1b	97.25	108.5
I_X , slug-ft ² I_Y , slug-ft ²	0.175	0.238 1.430
I_Z , slug-ft ²	0.910	1.430
$x_{ m cg}/l$ d, ft	0.343	0.245
l, ft	1.805	2.667
s, ft ²	0.348	0.348

TABLE II.- NOSE ORDINATES FOR MODEL II

x, in.	y, in.
0 .01 .10 .20 .30 .40 .50 .60 .80 1.00 1.50 2.00 2.50 3.00 3.50 4.00	1.600 2.198 2.765 2.964 3.086 3.177 3.249 3.309 3.406 3.483 3.627 3.733 3.817 3.887 3.947 4.000



TABLE III.- VALUES USED TO DETERMINE SLOPE OF NORMAL-FORCE COEFFICIENT

Mach number	ωΟ	λο	Δλ	Δω	$\frac{\frac{I_X}{I}\left(1 - \frac{I_X}{I_{+}I}\right)}{\left(1 - \frac{I_X}{2I}\right)^2}$	
Model I						
1.03	22.5	-1.33	0	2.75	0.224	
0.70	14.0	+0.57	0	1.95	0.224	
Model II						
2.07	37.0	-2.33	1.13	95.3	0.190	



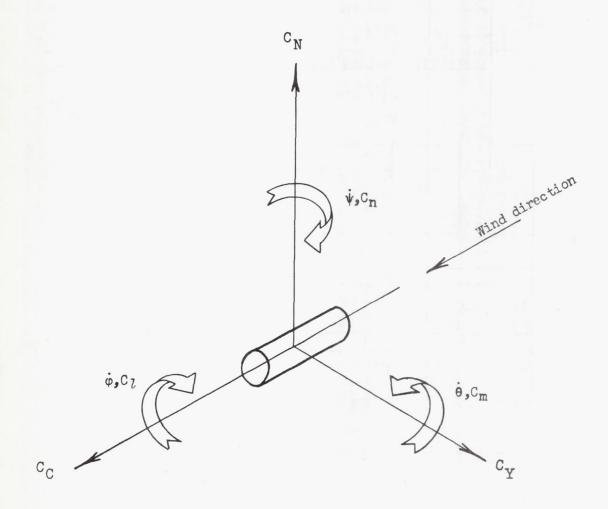
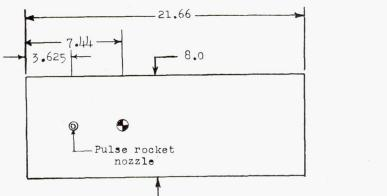
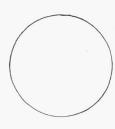


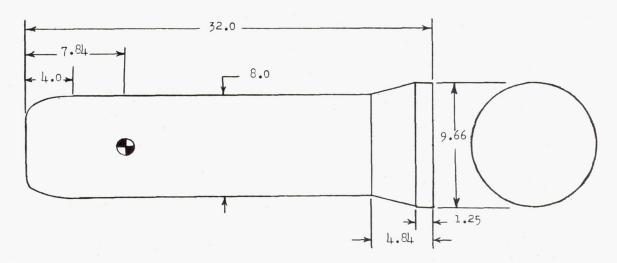
Figure 1.- Axes system showing positive directions of force and moment coefficients and angular velocities.







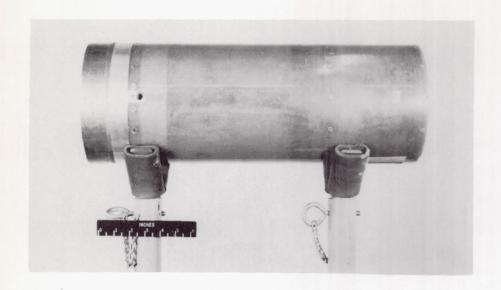
(a) Model I: Fineness-ratio-2.71 cylinder.



(b) Model II: Fineness-ratio-4.00 cylinder with a rounded nose and flared afterbody.

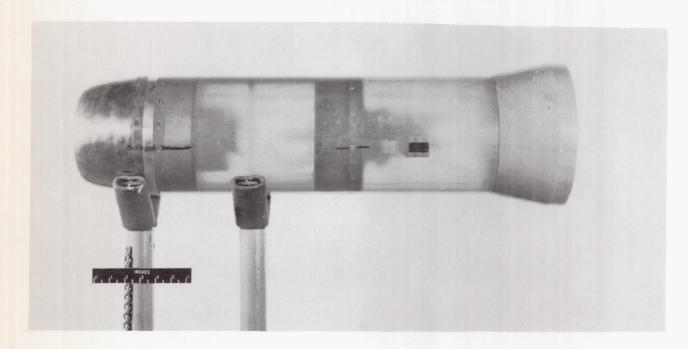
Figure 2.- Drawings of cylinders tested. All dimensions are in inches.





(a) Model I.

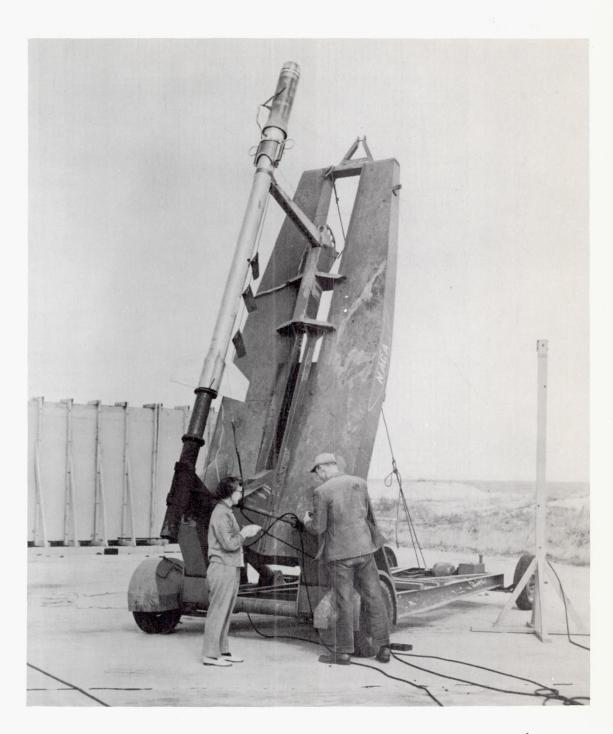
L-57-1733



(b) Model II. L-96363.1

Figure 3.- Photographs of cylinders tested.





(c) Model II on booster in launching position. L-57-1356.1 Figure 3.- Concluded.

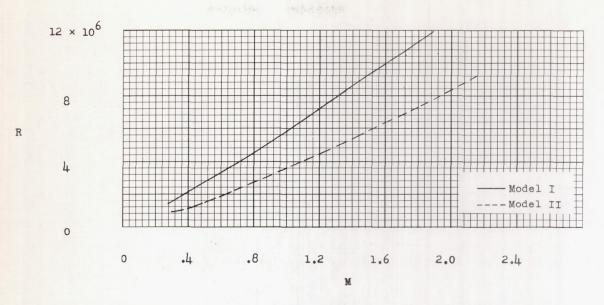


Figure 4. - Reynolds number of tests based on cylinder diameter.

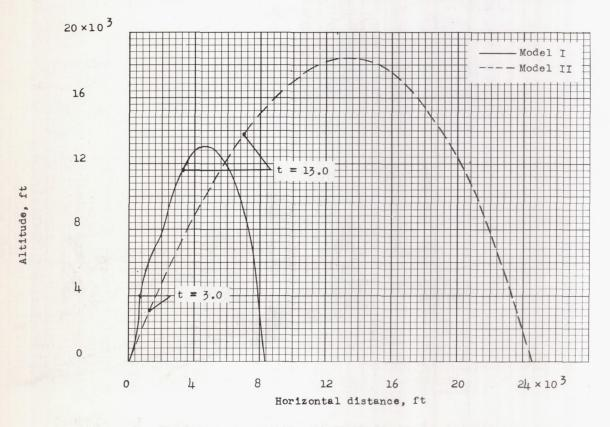


Figure 5.- Flight paths of cylinders tested.





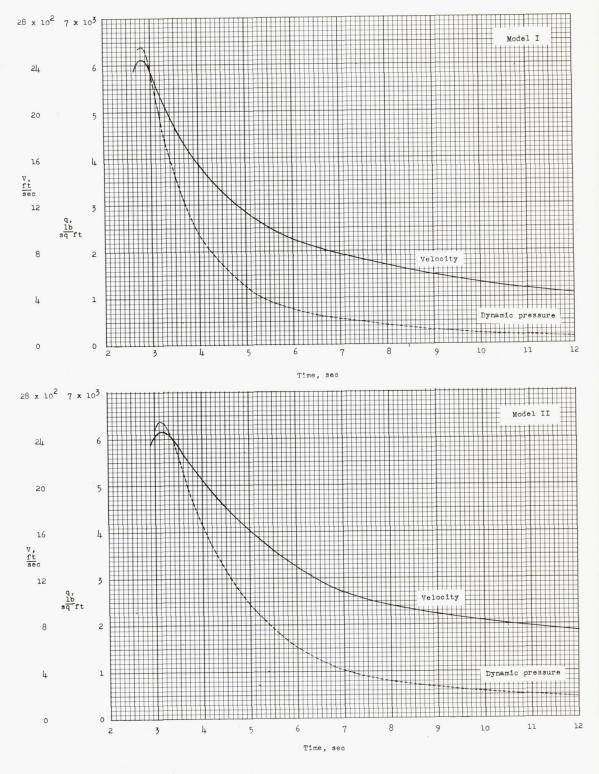


Figure 6.- Velocity and dynamic pressure of cylinders tested.



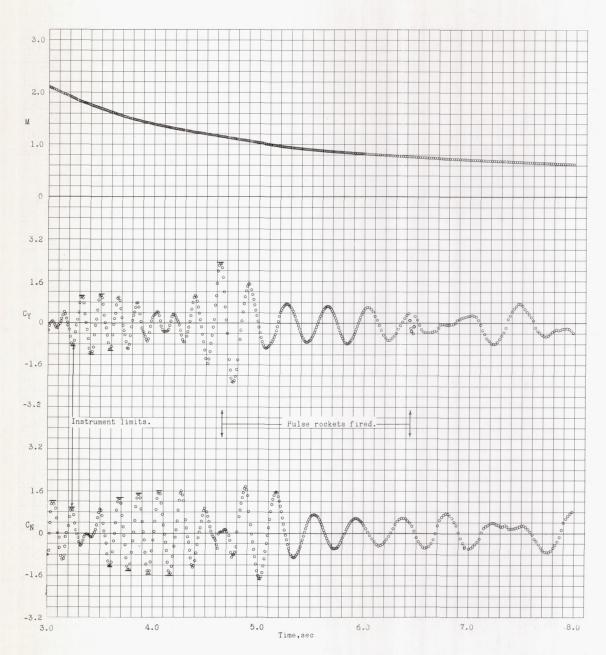


Figure 7.- Time history of fineness-ratio-2.71 cylinder. Model I.



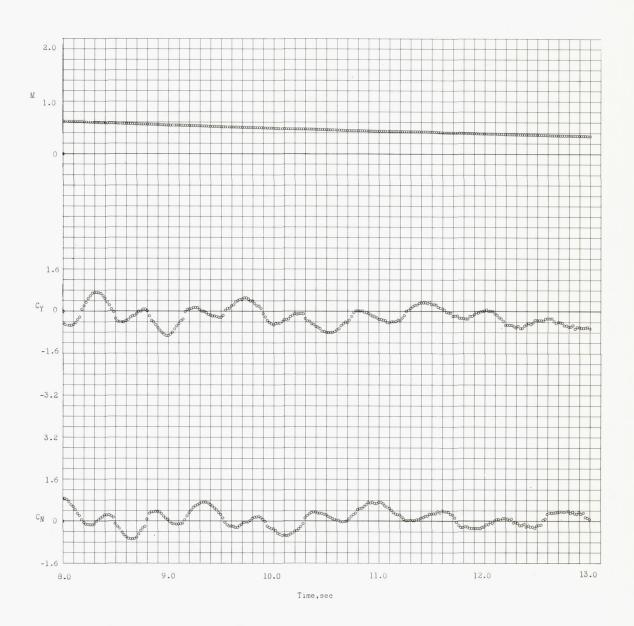


Figure 7.- Concluded.



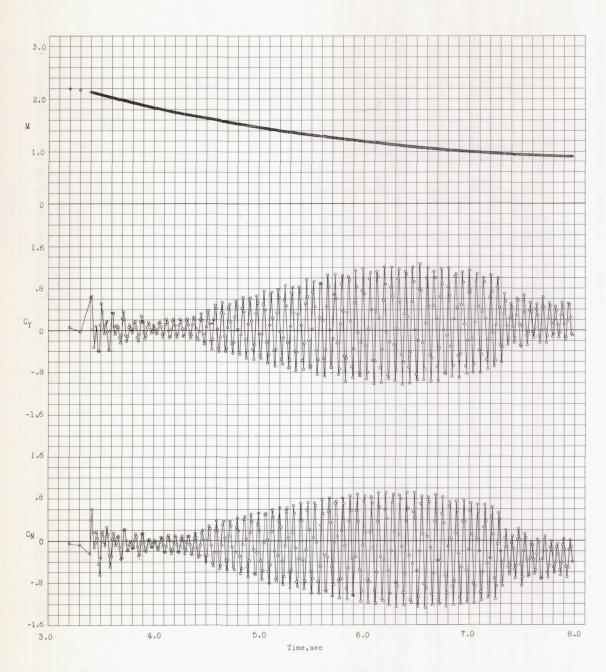


Figure 8.- Time history of fineness-ratio-4.00 cylinder with flared afterbody and rounded nose. Model II.



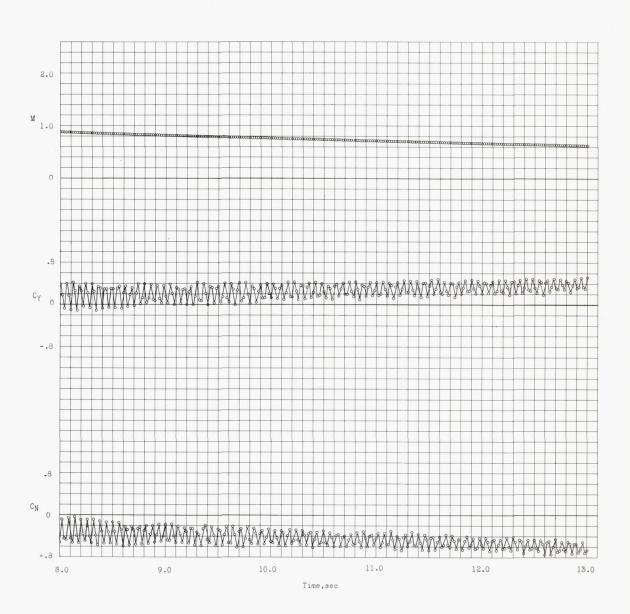


Figure 8. - Concluded.

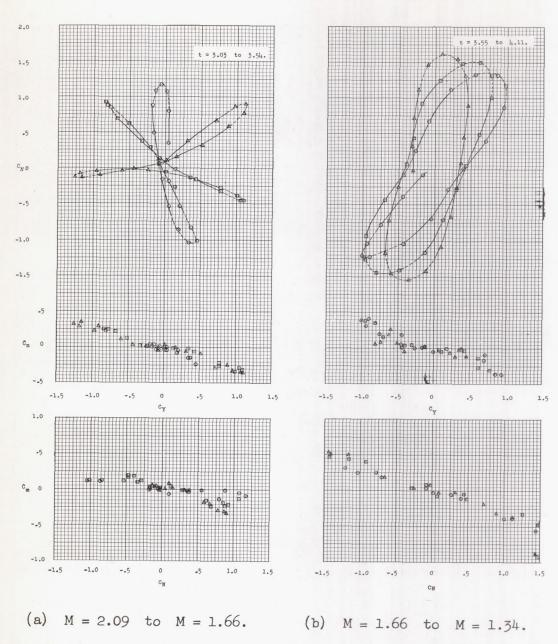
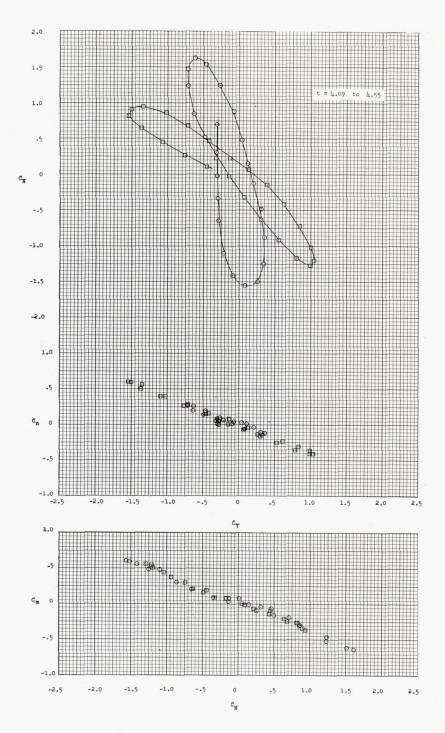
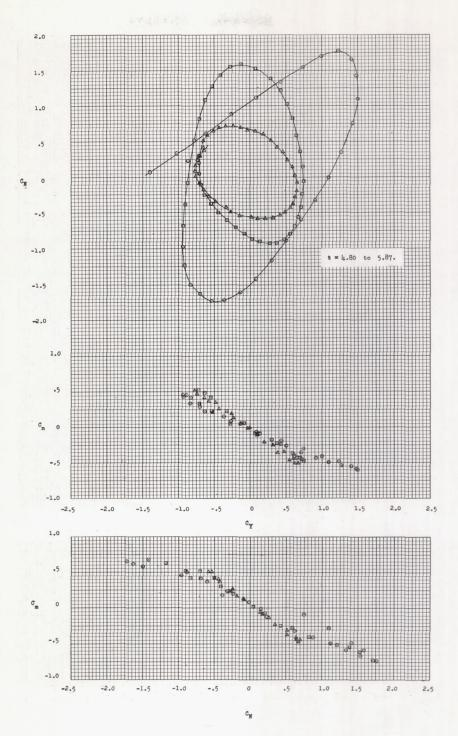


Figure 9.- Basic data cross plots of force and moment coefficients for the fineness-ratio-2.71 cylinder. Model I. The time sequence is indicated by the symbols \bigcirc , \square , and \triangle .



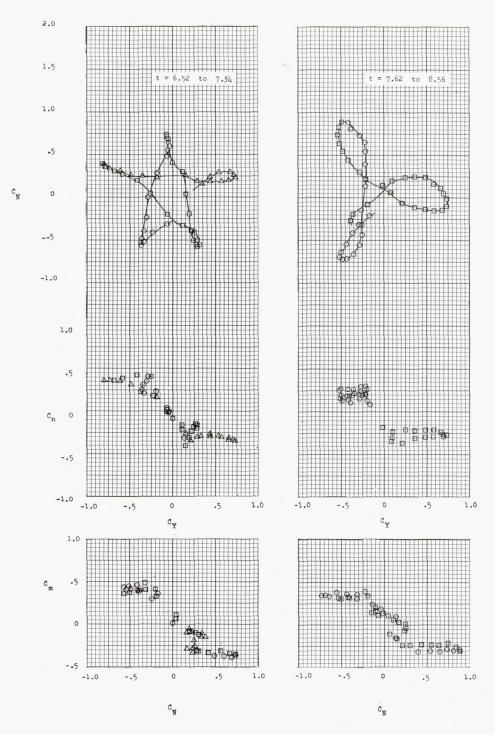
(c) M = 1.35 to M = 1.18. Figure 9.- Continued.



(d) M = 1.09 to M = 0.84.

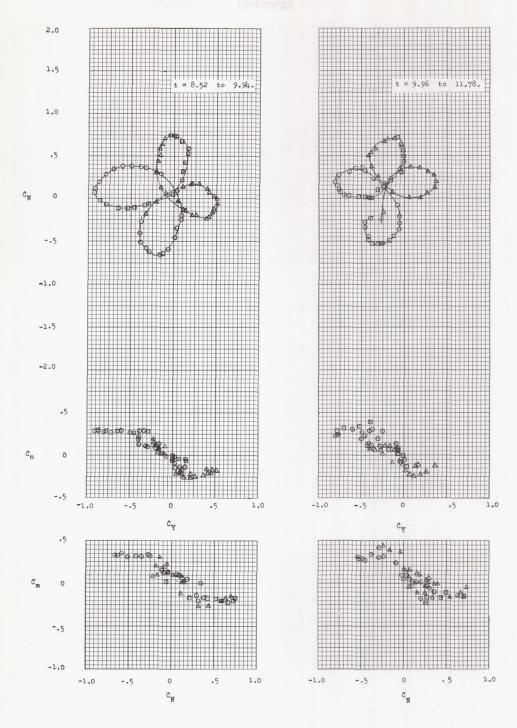
Figure 9. - Continued.





(e) M = 0.76 to M = 0.66. (f) M = 0.65 to M = 0.58. Figure 9:- Continued.



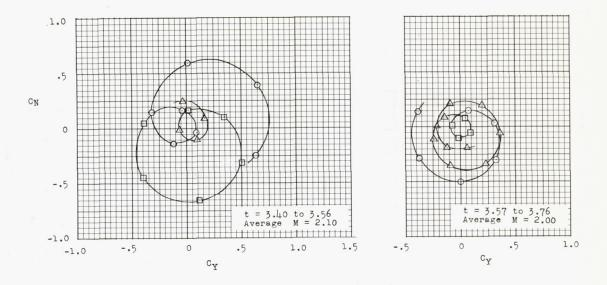


(g) M = 0.58 to M = 0.49. (h) M = 0.49 to M = 0.39.

Figure 9. - Concluded.







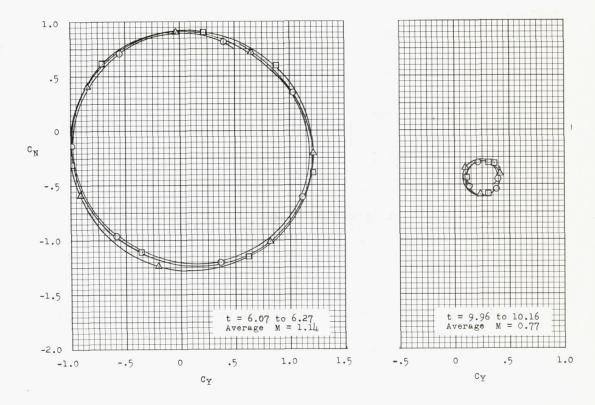


Figure 10.- Examples of force coefficients for the fineness-ratio-4.00 cylinder with flared afterbody and rounded nose. Model II. The time sequence is indicated by the symbols \circ , \Box , and Δ .



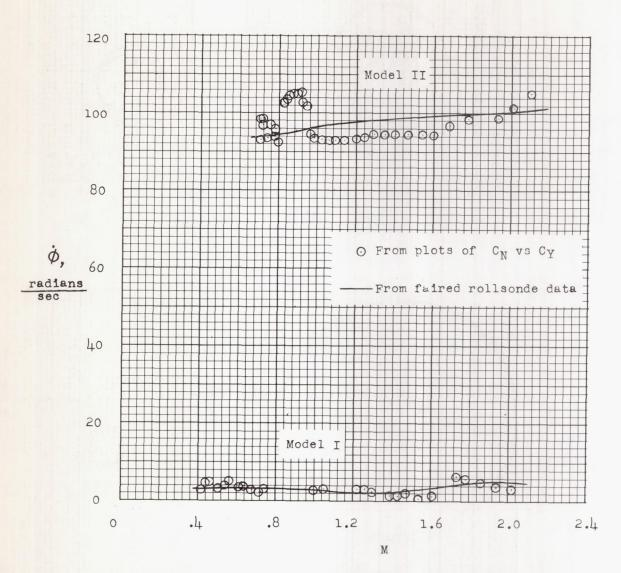


Figure 11. - Variation of rolling velocity with Mach number.



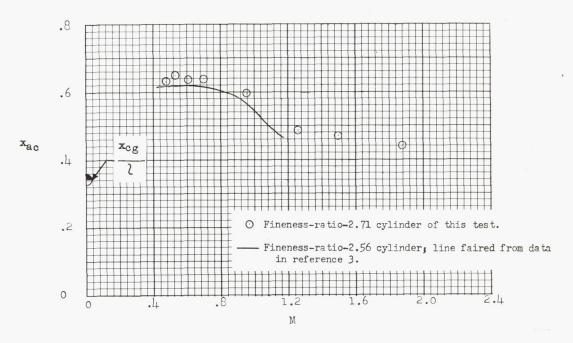


Figure 12. - Variation of aerodynamic center with Mach number.

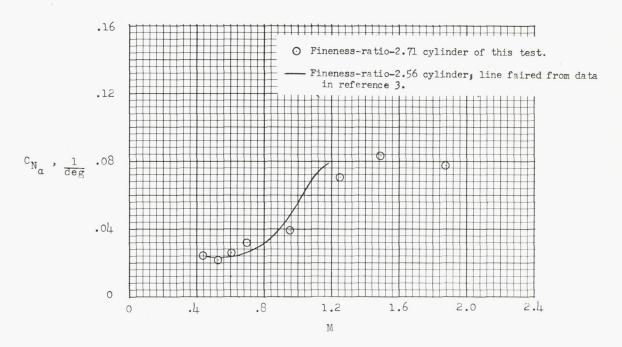
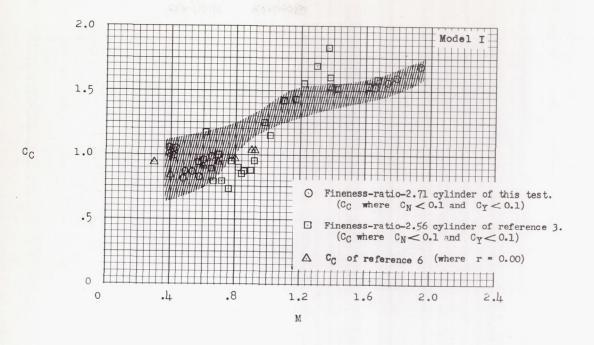


Figure 13.- Variation of normal-force coefficient slope with Mach number.

5



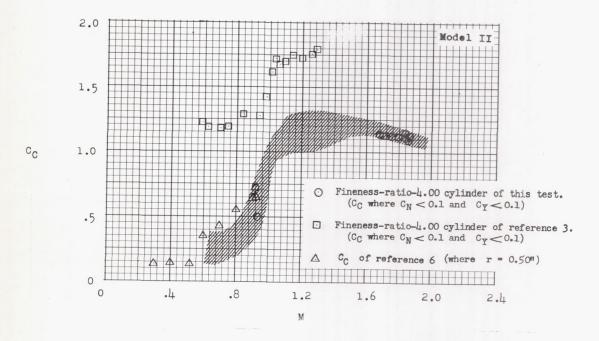


Figure 14.- Variation of longitudinal-force coefficient with Mach number. Shaded area indicates measured $\rm C_C$ for all $\rm C_N$ and $\rm C_Y$ values of this test.

